Published in final edited form as:

Adv Funct Mater. 2019 December 19; 29(51): . doi:10.1002/adfm.201904992.

Biodegradable fluorescent nanoparticles for endoscopic detection of colorectal carcinogenesis

Stephan Rogalla,
Molecular Imaging Program at Stanford University (MIPS), Department of Radiology, Stanford University School of Medicine, Stanford, CA 94305, USA

Department of Medicine (Gastroenterology & Hepatology), Stanford University School of Medicine, Stanford, CA 94305, USA

Krzysztof Flisikowski,
Chair of Livestock Biotechnology, Technische Universität München, Liesel-Beckmann Str. 1, D-85354 Freising, Germany

Dimitris Gorpas,
Helmholtz Zentrum München, German Researcg Center for Environmental Health, Institute of Biological and Medical Imaging, Ingolstädter Landstr. 1, D-85764, Neuherberg, Germany

Chair of Biological Imaging, TranslaTUM, Technische Universität München, Einsteinstr. 25, 81675, München, Germany

Aaron T. Mayer,
Molecular Imaging Program at Stanford University (MIPS), Department of Radiology, Stanford University School of Medicine, Stanford, CA 94305, USA

Department of Bioengineering, Department of Materials Science & Engineering, Stanford University, Stanford, CA 94305, USA

Tatiana Flisikowska,
Chair of Livestock Biotechnology, Technische Universität München, Liesel-Beckmann Str. 1, D-85354 Freising, Germany

Michael J. Mandella,
Molecular Imaging Program at Stanford University (MIPS), Department of Radiology, Stanford University School of Medicine, Stanford, CA 94305, USA

Institute for Quantitative Health Science and Engineering, Department of Biomedical Engineering, Michigan State University, 775 Woodlot Dr., East Lansing, MI 48824, USA

Xiaopeng Ma,

[*]**Corresponding Authors:** Prof. C. H. Contag contagch@msu.edu, Prof. S. S. Gambhir sgambhir@stanford.edu, and Dr. S. Harmsen sharmsen@protonmail.com.

Supporting Information

Supporting Information is available from the Wiley Online Library or from the author.

Conflict of Interest

S.H. is an inventor on a provisional patent that has been filed by the Office of Technology Transfer at Stanford University related to the design and application of biodegradable fluorescent nanoparticles for early endoscopic (pre)malignant lesion detection.

Helmholtz Zentrum München, German Researcg Center for Environmental Health, Institute of Biological and Medical Imaging, Ingolstädter Landstr. 1, D-85764, Neuherberg, Germany

Chair of Biological Imaging, TranslaTUM, Technische Universität München, Einsteinstr. 25, 81675, München, Germany

Kerriann M. Casey,
Department of Comparative Medicine, Stanford University School of Medicine, Stanford, CA 94305, USA

Stephen A. Felt,
Department of Comparative Medicine, Stanford University School of Medicine, Stanford, CA 94305, USA

Dieter Saur,
Department of Internal Medicine II, Klinikum Rechts der Isar, Technische Universität München, Ismaninger Str. 22, 81675, München, Germany

Vasilis Ntziachristos,
Helmholtz Zentrum München, German Researcg Center for Environmental Health, Institute of Biological and Medical Imaging, Ingolstädter Landstr. 1, D-85764, Neuherberg, Germany

Chair of Biological Imaging, TranslaTUM, Technische Universität München, Einsteinstr. 25, 81675, München, Germany

Angelika Schnieke,
Chair of Livestock Biotechnology, Technische Universität München, Liesel-Beckmann Str. 1, D-85354 Freising, Germany

Christopher H. Contag*,
Institute for Quantitative Health Science and Engineering, Department of Biomedical Engineering, Michigan State University, 775 Woodlot Dr., East Lansing, MI 48824, USA

Sanjiv S. Gambhir*,
Molecular Imaging Program at Stanford University (MIPS), Department of Radiology, Stanford University School of Medicine, Stanford, CA 94305, USA

Department of Bioengineering, Department of Materials Science & Engineering, Stanford University, Stanford, CA 94305, USA

Stefan Harmsen*
Molecular Imaging Program at Stanford University (MIPS), Department of Radiology, Stanford University School of Medicine, Stanford, CA 94305, USA

Abstract

Early and comprehensive endoscopic detection of colonic dysplasia – the most clinically significant precursor lesion to colorectal adenocarcinoma – provides an opportunity for timely, minimally-invasive intervention to prevent malignant transformation. Here, the development and evaluation of biodegradable near-infrared fluorescent silica nanoparticles (FSN) is described that have the potential to improve adenoma detection during fluorescence-assisted white-light colonoscopic surveillance in rodent and human-scale models of colorectal carcinogenesis. FSNs

are biodegradable ($t_{1/2}$ of 2.7 weeks), well-tolerated, and enable detection and delineation of adenomas as small as 0.5 mm^2 with high tumor-to-background ratios. Furthermore, in the human-scale, *APC*$^{1311/+}$ porcine model, the clinical feasibility and benefit of using FSN-guided detection of colorectal adenomas using video-rate fluorescence-assisted white-light endoscopy is demonstrated. Since nanoparticles of similar size (*e.g.*, 100–150-nm) or composition (*i.e.*, silica, silica/gold hybrid) have already been successfully translated to the clinic, and, clinical fluorescent/white light endoscopy systems are becoming more readily available, there is a viable path towards clinical translation of the proposed strategy for early colorectal cancer detection and prevention in high-risk patients.

Graphical Abstract

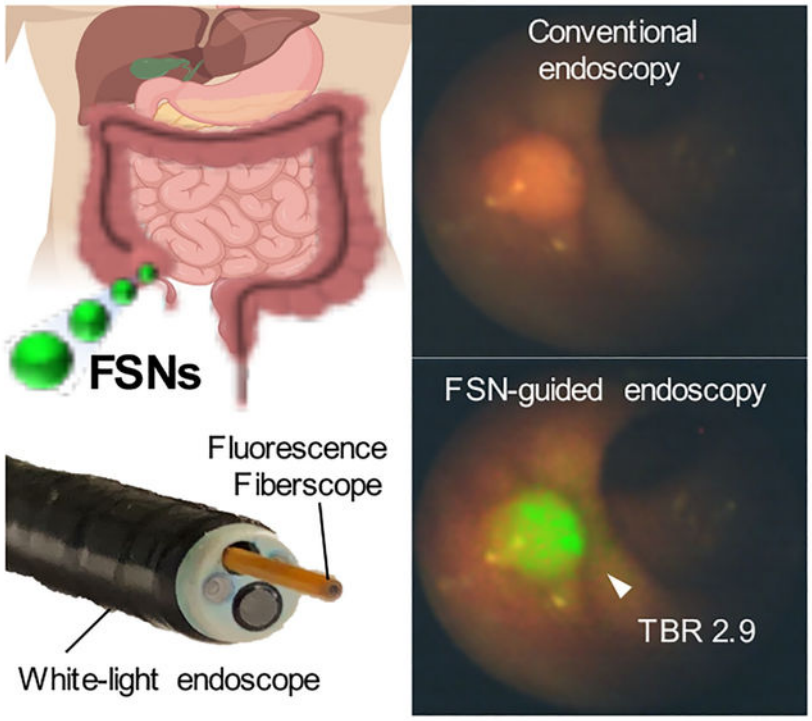

Table of Content figure.

Conventional white light colonoscopy has a relatively high adenoma miss rate particularly in high-risk patients. Biodegradable fluorescent silica nanoparticles (FSNs) have the potential to improve the detection of colorectal adenomas during endoscopic surveillance. Since FSNs are fully biodegradable and well-tolerated, there is a viable path towards clinical translation of FSN-guided colonoscopy for improved adenoma detection endoscopy in high-risk patients.

Keywords

Biodegradable; fluorescent nanoparticles; colorectal lesions; imaging; endoscopy

1. Introduction

Conventional white-light (WL) endoscopy plays a key role in the detection and removal of lesions of the digestive tract. In fact, early endoscopic detection and removal of (asymptomatic) colorectal dysplasia – the main precursor lesions of gastrointestinal (GI) cancers[1] – significantly reduces cancer risk and its associated death by 83% and 89%, respectively.[2] However, a substantial miss rate has been reported for WL detection of (pre)malignant lesions particularly in high risk patients (*e.g.*, inflammatory bowel disease, Lynch syndrome, *etc.*), which compromises early detection and intervention.[3] This significantly increases the risk of (interval) cancer and its associated mortality.[4] Important reasons for the miss rate are their subtle appearance that may appear nonpolypoid (flat or depressed), or lesions are located behind folds, or are not endoscopically identifiable altogether. Moreover, the subtle appearance complicates determination of the true lateral extent, thus impedes the ability to achieve complete endoscopic mucosal resection of these lesions resulting in recurrence rates of 15–26%.[5] Targeted biopsy using topically-applied dyes to delineate mucosal abnormalities (*i.e.* chromoendoscopy) has been shown to improve the adenoma detection rate by 30%.[6] However, chromoendoscopy is not embraced by endoscopists due to the perceived hassle, cost, and time associated with intraluminal dye administration,[7] and digital (image-enhanced) chromoendoscopy (*e.g.*, narrow-band imaging (NBI), Fuji Intelligent ChromoEndoscopy (FICE)) have only shown marginally improved adenoma detection rates.[8]

To mitigate the high miss-rate and low diagnostic accuracy of conventional white-light endoscopy, and, negate the perceived drawbacks of chromoendoscopy, we aimed to improve early detection of (incipient) colorectal cancer during endoscopic surveillance using nanoparticle-based optical contrast agents. The rationale was based on our observation that systemically administrated 100-nm Raman nanoparticles passively accumulated in a wide variety of tumors[9] including colorectal adenomas.[10] However, gold-based Raman nanoparticles are non-biodegradable and display long-term sequestration by the liver and spleen (>5 months) after intravenous administration. This may limit periodic, intravenous clinical application of these non-biodegradable Raman nanoparticles for routine screening in high-risk patients although topical administration within the bowel of targeted Raman nanoparticles may eventually be possible.

To benefit from the inherit tumoritropic properties of nanoparticles and address the issue of long-term sequestration, we developed biocompatible and biodegradable ‘nanosimilar’ near-infrared fluorescent silica nanoparticles. Evaluation in animal models of colorectal carcinogenesis demonstrated that fluorescent silica nanoparticles are biodegradable, well-tolerated, and, enable real-time detection of colorectal adenomas using near-infrared fluorescence-assisted white-light endoscopy (NIRF; here defined as excitation, emission >650nm) in transgenic rodent- and human-scale, porcine models of colorectal carcinogenesis. Furthermore, the fluorescent silica nanoparticles were designed to have optical properties that are fully compatible with existing clinical NIRF/WL endoscopy systems to facilitate clinical translation.

2. Results

2.1 Synthesis and characterization of fluorescent silica nanoparticles

Biodegradable fluorescent silica nanoparticles were synthesized using a modified Stöber reaction in the presence of a (3-mercaptopropyl)trimethoxysilane-appended near-infrared dye (CF680R-MPTMS) to ensure covalent incorporation of the dye into the silica nanoparticle matrix (Figure S1). A CF680R-MPTMS concentration of 0.75 μM proved to be optimal and reproducibly yielded near-infrared fluorescent silica nanoparticles with the highest fluorescence intensity on a per particle basis (Figure S2 and S3). The surface of these nanoparticles was modified using MPTMS to introduce thiol-functionality, which, in turn, was used for passivation of the nanoparticle surface with hydroxy-terminated polyethylene glycol (PEG-OH; 3.4 kDa) via straightforward maleimide chemistry. The zeta potential of the bare fluorescent silica nanoparticles and PEGylated fluorescent silica nanoparticles – from here on termed FSNs – was measured to be −41.8±6.3 mV and −20.2 ±7.0 mV, respectively. As shown in Figure 1, the silica core of the FSNs had a size of 100 nm as determined by transmission electron microscopy (TEM). Following PEGylation with hydroxy-terminated PEG (3.4 kDa), the hydrodynamic diameter of the FSNs increased by 17 nm. The Flory radius of ~8.5 nm indicate that the PEG chains had assumed a brush-confirmation,[11] which has been shown to be significantly more resistant to plasma protein adsorption.[12] In fact, when incubated for 1 h in human serum, less protein had adsorbed to the FSNs (PEG-OH grafted) *versus* bare fluorescent silica nanoparticle cores (Figure S4). The FSNs had an excitation maximum that was red-shifted 10 nm relative to the silane-appended CF680R dye and were shown to have a limit of detection of 10 femtomolar (10×10^{-15} M), which was an order-of-magnitude higher than our previously described Raman nanoparticles that have a non-biodegradable gold nanocore.[9] To validate the biodegradation of FSNs *in vitro*, FSNs were incubated in 50% (w/v) human serum at 37 °C (Figure 1). As shown by TEM, within 10 days the FSNs etched from the inside and started to collapse signifying the biodegradation of FSNs under physiological conditions (Figure 1e).

2.2 In vivo biodegradability of non-PEGylated FSNs and FSNs

To determine the *in vivo* biodegradation kinetics of FSNs, we intravenously (i.v.) injected nude mice either with non-PEGylated FSNs, an equimolar amount of FSNs, or 5% (w/v) D-glucose in water (D5W) as a vehicle control (n=5 per group). The administrated FSN dose of 30 fmol g^{-1} was equivalent to the dose of Raman nanoparticles that was used in our previous study.[10] We performed the biodegradation study in nude mice to allow longitudinal monitoring of hepatic near-infrared fluorescence in the same animals over a 6-month time period post systemic FSN administration. As shown in Figure 2, 1-d post injection (‘0’ time point) of an equimolar dose of fluorescent nanoparticles, the biodistribution of the non-PEGylated FSNs *versus* FSNs was distinct. While the non-PEGylated demonstrated mostly hepatic uptake, FSNs distributed to the liver and spleen. Based on the loss of significance between the hepatic fluorescence intensity of the injected animals compared to the background fluorescence in naïve animals (Figure 2b), it was concluded that the FSNs and non-PEGylated FSNs fully degrade and clear within 3-months ($t_{1/2}$ 2.7 weeks) and 4-months ($t_{1/2}$ 3.0 weeks) post injection, respectively. TEM demonstrated a biodegradation pattern of the FSNs *in situ* that was similar to that observed *in vitro* with the FSNs etching from the

inside, collapsing, and dissolving (Figure S5). To ensure that the decrease in fluorescence signals was due to FSN biodegradation and clearance, and not due to photobleaching resulting from the repeated imaging, we included a standard that contained a dilution series of the exact same batch of fluorescent silica nanoparticles as the one that was injected. The coefficient of variance (CV) of the near-infrared fluorescent signal was <5% over the 6 months period (~200 exposures) indicating the fluorescent silica nanoparticles should be photostable and the decrease in hepatic fluorescence signal should not be due to photobleaching (Figure S6).

Throughout the biodegradation study, the animals were closely monitored, and no overt signs of pain or distress were observed. Following the biodegradation study, all animals were humanely euthanized, and major organs (*i.e.*, liver, spleen, kidney) were harvested and submitted for histopathological assessment. No abnormalities were found in the inspected organs after long-term exposure to the FSNs indicating that the non-PEGylated FSNs as well as the PEGylated FSNs were well-tolerated at the current dose (Figure S7).

2.3 Detection of adenomas in the intestinal tracts of $Apc^{Min/+}$ mice

We used the $Apc^{Min/+}$ mouse model of familial intestinal carcinogenesis to determine the ability of FSNs to enable detection and visualization of intestinal adenomas. The $Apc^{Min/+}$ mice (n=5) received 75 μL of 10 nM FSNs in D5W to achieve a dose of 30 fmol g^{-1} via i.v. injection. Since the $Apc^{Min/+}$ mice most commonly develop adenomas in the small intestine,[13] the intestinal tracts of the injected animals were harvested and imaged 1-day post injection. As shown in Figure 3, FSNs enabled instant, wide-field near-infrared fluorescence (NIRF) imaging of freshly resected ileal tissues. The tumor-to-background ratio (TBR) of selected polyps was >3 and polyps as small as 0.5 mm^2 (lesion 3) were detected. Histopathological assessment of the tissues by a veterinary pathologist identified the FSN-positive lesions as adenomatous polyps. Since hematoxylin and eosin do not fluoresce >700 nm, we performed NIRF imaging of the H&E-stained tissue sections and verified the presence of the FSNs in the adenomatous polyps after intravenous administration in $Apc^{Min/+}$ mice (Figure 3c).

To probe the intratumoral fate of the intravenously injected FSNs, we performed high magnification NIRF confocal microscopic imaging on the H&E stained tissue section of the adenoma. It was shown that upon extravasation, the FSNs specifically localize to and reside within the stromal compartment of the adenoma and do not readily interact with the epithelial cells lining the adenoma. Furthermore, within the tumor stroma the FSNs were found to be mostly associated with neutrophils and tumor-associated macrophages (Figure 3e and S8).

2.4 FSN-augmented endoscopic detection of dysplastic colorectal lesions in $Apc^{Pirc/+}$ rats

To assess the ability of FSNs to highlight colorectal adenomas in a preclinical endoscopic scenario, we used the $Apc^{Pirc/+}$ rat animal model. In contrast to the $Apc^{Min/+}$ mouse model, $Apc^{Pirc/+}$ rats do predominantly develop adenomas and localized adenocarcinomas in the colon.[14] Furthermore, the larger body size of the rats enabled the accommodation of the

endoscope to perform endoscopic colonic surveillance. The endoscopy system constituted a clinical white-light endoscope that is equipped through its working-channel with an FDA-cleared Spyglass fiberoptic probe (Figure S9).

Combined NIRF/WL endoscopy was performed in $Apc^{Pirc/+}$ rats (n=5) that had received i.v. doses of FSNs (30 fmol g^{-1}) 18 h prior to endoscopy. As shown in Figure 4a and Movie S1, FSNs highlighted adenomas during NIRF/WL endoscopic surveillance of the colon in these animals. Of note, the signal produced by the FSNs was sufficiently high to enable real-time endoscopic surveillance at a frame-rate of at least 5.0 frames per second (fps). To validate the NIRF/WL endoscopy findings, the colons were collected, dissected, and imaged on a wide-field NIRF imaging system immediately after endoscopic surveillance. The wide-field NIRF imaging supported the NIRF/WL endoscopy findings and demonstrated that the FSNs predominantly accumulated in colorectal adenomas (Figure 4, Figure S10, Table S1). Of note, upon closer inspection of the H&E stained tissue section of the smaller adenoma ('1'), it was shown to have a mixed morphology of a hyperplastic polyp and adenoma with an isolated dysplastic focus. NIRF microscopy of this mixed hyperplastic adenomatous polyp demonstrated that the presence of FSNs was only associated with the stromal compartment of the dysplastic focus and not with that of the surrounding hyperplastic and normal colorectal tissues (Figure 4c).

As shown in Figure S10 and Table S1, guided pathological assessment of the NIRF-positive lesions (n=27) demonstrated that 21 of these lesions were true positives (*i.e.*, adenomas) and 6 were falsely positive (*i.e.*, Peyer's patches (n=5) or of unknown status (n=1)). Furthermore, 2 NIRF-negative sections (Figure S10a–d; sections 3) that were subjected to histological assessment were both true negatives (*i.e.*, no adenomas were present). Although no abnormalities (*i.e.*, polyps) were noted under gross visual inspection of all the resected colorectal tissues other than the adenomas that were highlighted by the FSNs, we cannot exclude the presence of any (microscopic) false negatives. A positive predictive value of 78% was calculated based on this relatively small number of specimens.

2.5 FSN-augmented endoscopic detection of dysplastic colorectal lesions in the human-scale $APC^{1311/+}$ porcine model of colorectal carcinogenesis

FSNs are not yet approved in humans for colorectal dysplasia detection. Therefore, to assess clinical feasibility of our approach, we performed a large animal study in a human-scale model of colorectal carcinogenesis − the $APC^{1311/+}$ porcine model.[15] $APC^{1311/+}$ pigs carry a gene mutation orthologous to a common germline mutation found in human FAP patients (*i.e.* APC^{1309}) and develop high-grade dysplastic colorectal adenomas in a similar manner as human patients with familial adenomatous polyposis (FAP) or sporadic colorectal cancer.[15–16] Based on allometric scaling of the rodent dose (30 fmol g^{-1}), a dose of ~5 fmol g^{-1} was selected for administration to the $APC^{1311/+}$ pigs.[17] Accordingly, two $APC^{1311/+}$ pigs weighing 79 and 94 kgs received an intravenous injection of 15 mL 25 nM FSNs in D5W to achieve a dose of 4.7 and 4.0 fmol g^{-1}, respectively. The next day, the colons of the anesthetized animals were surveilled using combined NIRF/WL endoscopy (Figure 5, S9 and Movie S2). At the selected dose, the FSNs highlighted the adenomas and enabled real-time, combined NIRF/WL surveillance at a frame-rate of at least 5.0 fps. Following

endoscopy, one animal (with weight 94 kg) was sacrificed and its colons was harvested, and formalin fixed. The fixed tissue was subjected to wide-field NIRF imaging (Figure 5). The adenomatous polyps were highlighted by the FSNs during wide-field NIRF imaging and demonstrated TBRs of >1.3. Histopathological assessment of the FSN-positive lesions by a trained and certified veterinarian pathologist proved the lesions were adenomatous polyps.

3. Discussion

We developed biodegradable fluorescent silica nanoparticles (FSN) that are well-tolerated and highlight colorectal adenomas − the most clinically significant precursor lesions to colorectal adenocarcinoma[1] − during video-rate, near-infrared fluorescence-assisted white-light colonoscopic surveillance in small- and human-scale animal models of colorectal carcinogenesis. The presented advantages of our FSN-based strategy to highlight adenomas during fluorescence-assisted white-light colonoscopy are aimed at improving the miss rate of colonoscopy, and to address the perceived hassle, cost, and time associated with intraluminal dye administration for chromoendoscopy.[7, 18]

In recent years, several targeted, molecular imaging strategies have been investigated to highlight colorectal lesions during fluorescence-assisted white-light endoscopy. Most notably, vascular endothelial growth factor (VEGF) or epidermal growth factor receptor (EGFR) targeting antibodies or c-MET targeting peptides labeled with NIRF dyes to minimize tissue autofluorescence,[19] have shown great promise in improving adenoma detection during fluorescence-assisted white-light colonoscopy in the clinic.[20] However, often active targeting approaches are limited by target (over)expression and heterogeneity, specificity, and accessibility at the tumor site.[20b, 21] For instance, EGFR is overexpressed in 50% of colorectal adenomas and heterogeneously expressed in those EGFR-positive lesions.[22] Moreover, since target expression may not be tumor stage-specific it may lead to over-diagnosing, as illustrated in a clinical trial with an intravenous c-Met targeting probe that not only highlighted colorectal adenomas, but also hyperplastic polyps, which have no clinical relevance.[23]

In contrast to active targeting approaches, passive tumor targeting using fluorescent dye-embedded nanoparticles (>10 nm) obviates the need for specific targeting moieties, because tumor accumulation is governed by a biologically phenomenon that is shared by lesions across the cancer spectrum ranging from dysplastic- to advanced malignant diseases; the enhanced permeability and retention (EPR) effect.[24] The enhanced permeability of the tumor neovasculature facilitates extravasation of nanoparticles into the tumor bed where they are locally retained due to ineffective lymphatic drainage.[25] Since it has been shown that EPR strongly correlates with the degree of tumor vascularization[26] and dysplastic colorectal lesions commonly have increased vascularity,[27] nanoparticles such as Raman nanoparticles and FSNs can specifically accumulate in clinically relevant dysplastic lesions.[10]

Unlike the Raman nanoparticles, however, FSNs consist solely of dye-embedded silica – a biocompatible and biodegradable material that has already been translated to the clinic.[28] In addition, FSNs have a detection limit that is only one order-of-magnitude higher than that

of Raman nanoparticles, which to date have showcased the lowest reported limit of detection using (near) real-time optical imaging[9, 29]. Relative to other fluorescent-based agents such as free- or targeted dyes (*e.g.* indocyanine green (ICG), IRdye800CW, respectively) or liposomal dye formulations, which typically have a limit of detection in the picomolar range (10^{-12} M), FSNs have a limit of detection in the low femtomolar range (10^{-14} M; Figure 1a). Covalently-incorporated dyes within the silica matrix exhibit photophysical properties that are distinct from their solution properties, thereby leading to enhanced radiative emission and increased photostability[30].

Our studies were performed in genetically engineered rodent and human-scale, porcine models of gastrointestinal carcinogenesis – the $Apc^{min/+}$ mouse, $Apc^{Pirc/+}$ rat, and $APC^{1311/+}$ pig. The rodent models have been criticized for not (or rarely) progressing to invasive carcinoma,[31] which is as yet an open question for the porcine models. However, in all species the lesions develop via the Vogelstein-sequence,[32] and, as such, the *Apc*-driven carcinogenesis animal models are particularly useful for our purpose of evaluating endoscopic detection of dysplastic lesions using FSNs. In fact, we demonstrated that after intravenous administration the FSNs enable detection of colorectal adenomas as small as 0.5 mm^2 throughout the intestinal tract of $Apc^{Min/+}$ mice and in the larger $Apc^{Pirc/+}$ rat- and $APC^{1311/+}$ porcine model. A positive predictive (PPV) value of 78% was determined. However, this number is likely higher for FSN-guided endoscopy. Unlike (epi-)fluorescence wide-field NIRF imaging, which was used here to establish the PPV, where the tissue is illuminated at a 90° angle, fluorescence endoscopic imaging is performed along the luminal surface at a 145°–180° angle. In this way, only superficial mucosal lesions will be detected and not Peyer's patches, which are located in the deeper submucosal tissue layer.

Widespread improvement in the endoscopic recognition of colorectal adenomas will have important implications for the surveillance and management of incipient colorectal cancers and cancer prevention. Our proposed use of intravenous FSNs as positive contrast agents for endoscopic detection of (pre)malignant lesions of the GI tract is fully compatible with current clinical practice and instrumentation. For instance, an intravenous bolus injection can be administered during the obligate blood-draw procedure prior to endoscopic surveillance. Furthermore, since the FSNs are fully biodegradable, they can be used routinely in high-risk patients. Lastly, the TBRs produced by FSN-augmented fluorescence-assisted endoscopy enables a binary ("yes or no") read-out to reduce interoperator variability, improve (pre)malignant lesion detection and diagnostic accuracy, and enable targeted sampling and resection of visualized lesions to allow a shift in practice away from the random biopsy technique, where less than 0.1% of the mucosal surface area is blindly sampled, and away from aggressive intervention (*e.g.*, colectomy) for the management of dysplasia in high-risk patients.

4. Conclusion

In conclusion, we have developed a biodegradable fluorescent nanoparticle that highlights dysplastic adenomas in animal models of colorectal carcinogenesis. With clinical translation in mind, future studies will be aimed at dose de-escalation and long-term toxicity risk assessment. The FSN dose that was used throughout the reported study was based on the

Raman nanoparticle dose as reported in a previous study.[10] Therefore, to find the minimum effective dose, we will perform FSN dose de-escalation studies and determine the lowest dose at which adenomas are still detectable using FSN-enhanced NIRF/WL colonoscopy. Furthermore, since we aim at early colorectal disease detection in high-risk patients, who undergo routine (*e.g.*, annual) screening to monitor disease development or progression, we will study the effect of FSN dose accumulation on organs of the mononuclear phagocyte system (*e.g.*, liver, spleen, bone marrow), which avidly take up FSNs following intravenous administration. Although we did not observe any acute toxicity in the liver, spleen, and bone marrow following a single intravenous administration of FSNs, long-term toxicity effects following single or repetitive FSN administration remain to be explored.

5. Experimental Section

Materials:

All chemicals were purchased from Sigma-Aldrich (St. Louis, MO) unless stated otherwise, were of the highest purity available, and used without any further purification.

Fluorescent silica nanoparticle (FSN) synthesis:

CF680R-maleimide (1 μmol in 100 μL dry *N*,*N*-dimethylformamide (DMF); Biotium Inc., Fremont, CA) was reacted with (3-mercaptopropyl)trimethoxysilane (MPTMS; 2 μmol) to yield silane-appended CF680R (CF680R-MPTMS), which was used without any further purification. Typically, CF680R-MPTMS (4 μL 10 mM in DMF) was added to 2-propanol (50 mL) containing water (3.5 mL), ammonium hydroxide (1.5 mL 28% v/v), and tetraethyl orthosilicate (TEOS, 2.5 mL 99.999% v/v). After 15 min, the fluorescent silica nanoparticles were collected by centrifugation (10 min; 7,500 *g*; 20°C), washed with excess ethanol, and redispersed in ethanol (2.5 mL) containing ammonium hydroxide (50 μL 28% v/v) and MPTMS (150 μL 95% v/v). After 90 min at ambient conditions, the thiol-functionalized FSN were washed with excess ethanol. The thiol-functionalized FSNs were stored in ethanol at 4°C. On the day of injection, the thiol-functionalized FSNs were collected by centrifugation and redispersed in 3-(*N*-morpholino)propanesulfonic acid buffer (MOPS; 2 mL 10 mM; pH 7.3) containing maleimide-functionalized hydroxyl-terminated polyethylene glycol (PEG-OH; M_w 3,400 da; 3.5 mg; Creative PEGWorks, Chapel Hill, NC) and allowed to react for at least 2 h at ambient conditions. The PEG-OH functionalized fluorescent silica nanoparticles (FSN)s were purified and redispersed in 1.0 mL 22-μm filter-sterilized 5% D-glucose (D5W) at a concentration of 10 nM.

FSN characterization:

FSN size/integrity, hydrodynamic diameter/concentration, and limit of detection were characterized using transmission electron microscopy (TEM), nanoparticle tracking analysis (NTA), and near-infrared fluorescence (NIRF) imaging, respectively. In brief, 1 μL of an FSN dispersion was pipetted onto a carbon-coated grid (CF300-Cu, Electron Microscopy Sciences), air-dried, and loaded into an JEOL 1200ex-II transmission electron microscope operating at 80 kV. The hydrodynamic diameter and concentration of FSNs were determined using NTA using a 1000-fold diluted sample of an FSN dispersion in water. The limit of detection of FSNs was determined by imaging a concentration series of FSNs (3-fold

dilution factor) on a Pearl Trilogy NIRF imaging system (LI-COR Biosciences, Lincoln, NE). The excitation and emission curves of CF680R-MPTMS and FSNs in ethanol were measured on a Spark® fluorescence spectrophotometer (Tecan, Männedorf, Switzerland). Emission curves were measured upon 676 nm and 686 nm excitation, which are the excitation maxima of CF680R and FSNs, respectively. The zeta potential of 5.0 nM dispersion of non-PEGylated and PEGylated FSNs in 0.22-μm filtered 20 mM MOPS (pH 7.3) was measured using a Zetasizer Nano ZS (Malvern). Biodegradation of FSN was verified *in vitro*. FSNs (1.0 nM) were incubated in human serum (250 μL 50% w/v) at 37 °C. At days 0, 3, 6, and 9, 50 μL was sampled, washed with excess water, collected using centrifugation (10,000*g*), and analyzed using TEM.

In vivo study:

The *in vivo* studies at Stanford University (*i.e.* mouse and rat) were conducted under an Institutional Animal Care and Use Committees (IACUC)-approved protocols (#27715 and #30122) and animals were under the direct oversight of an animal care and use program that was AAALAC International-accredited and PHS-assured. The *in vivo* studies in the porcine model were performed at the Technical University of Munich and were approved by the Federal Government of Bavaria (R OB55.2-2-2532.Vet_02-18-33). All applicable institutional guidelines for the care and use of animals were followed. Athymic nude mice (Charles River Laboratories, Wilmington, MA), $Apc^{Min/+}$ mice (Jackson Laboratory, Bar Harbor, ME), and $Apc^{Pirc/+}$ rats (Rat Resource & Research Center, Columbia, MO) were fed Teklad Global 2018 diet (Envigo, Huntingdon, UK), which contains 18% (w/w) protein, 6% (w/w) fat, moderate phytoestrogens and no alfalfa. $APC^{1311/+}$ pigs were fed a normal diet. The formalin fixed colorectal porcine tissues were imported from Germany to Stanford, CA under UNITED STATES VETERINARY PERMIT FOR IMPORTATION AND TRANSPORTATION OF CONTROLLED MATERIALS AND ORGANISMS AND VECTORS (USDA Permit Number 136396).

Biodegradability and biocompatibility:

Non-PEGylated, thiol-functionalized fluorescent silica nanoparticles or FSNs grafted with PEG-OH (3.4 kDa) in D5W were intravenously administered at a dose of 30 fmol g^{-1} to 2-month old, female nude mice (n=5 per group). A separate group of 2-month old, female nude mice (n=5 per group) received an intravenous injection of the vehicle D5W. After 24 h, the animals were imaged (t='0') on a small animal NIRF imaging system (Pearl Trilogy, LI-COR Biotechnology, Lincoln, NE). Following monthly imaging for 6 months, the animals were euthanized by CO_2 asphyxiation and cardiac exsanguination. Select tissues (liver, spleen, kidney, and bone marrow) were harvested and immersion-fixed in neutral-buffered formalin (10% w/v) for 72 h. Femurs were harvested for bone marrow analysis and immersion-fixed/decalcified in Cal-Ex II Fixative/Decalcifier (Fisher Scientific, Fair Lawn, NJ, USA) for 72 h. Formalin-fixed tissues were processed routinely, embedded in paraffin, sectioned at 5 μm, and stained with hematoxylin and eosin (H&E). H&E sections were blindly evaluated by a board-certified veterinary pathologist (KMC) for treatment-related toxicity. Of note, a small section of the liver and spleen of selected animals was fixed in electron microscopy fixative (2% (v/v) glutaraldehyde, 4% (w/v) paraformaldehyde in 0.1 M sodium cacodylate; pH 7.4) and submitted to Stanford Microscopy Facility for transmission

electron microscopy analysis. Tissue sections were counterstained and imaged on a JEOL JEM-1400 operating at 120 kV.

Detection of adenomas in $Apc^{Min/+}$ mice:

Conscious female $Apc^{Min/+}$ mice (14–20-week old; n=5) received intravenous injections of FSNs (30 fmol g^{-1}) via the tail vein using a tail-restrainer. The next day, the animals were deeply anesthetized using inhalant isoflurane (Forane, Baxter, Deerfield, Il) and then euthanized via cervical dislocation. The intestinal tissues of the animals were immediately collected, rinsed with PBS and immediately imaged on a Pearl Trilogy NIRF imaging system. Upon completion of imaging, the intestinal tissues were immersion-fixed in neutral-buffered formalin (10% v/v) for 24 h and processed for paraffin-embedding and H&E staining. H&E stained tissue section (5- and 15-μm thickness) were re-imaged on an Odyssey NIRF imaging system (Pearl Trilogy, LI-COR Biotechnology, Lincoln, NE) and BZ-X700 NIRF microscope (Keyence, Itasca, Il).

Fluorescence-activated cell sorting (FACS) of FSN-associated cells within polyps:

Conscious female $Apc^{Min/+}$ mice (18-week old; n=2) received intravenous injections of FSNs (30 fmol g^{-1}) via the tail vein using a tail-restrainer. The next day, the animals were deeply anesthetized using inhalant isofluorane and then euthanized by cervical dislocation. Small intestinal tissue containing adenomas was collected and sectioned into small (2–3 mm) pieces and then placed in a dounce glass homogenizer to create a cell suspension. Cells were passed through a 40-μm filter with Hank's balanced salt solution (HBSS) containing DNAse. Cells were counted and resuspended in PBS at a concentration of 1×10^6 cells, prior to live dead staining with fixable LD aqua (#L34957, ThermoFisher Scientific, Waltham, MA) for 15 min. Cells were then washed and resuspended in PBS containing 2% bovine serum albumin (BSA), prior to staining with the fluorophore conjugated antibody panel (Pacific Blue anti-human CD11c (1:40; 117321), R-phycoerythrin (PE)-Cy7 anti-human Ly-6G (1:40; 127618), Allophycocyanin (APC)-Cy7 anti-human CD11b (1:40; 101225), PE anti-human CD3 (1:40; 100206), Peridinin-Chlorophyll protein (PerCP)-Cy5.5 anti-human CD45 (1:40; 103132); Biolegend, San Diego, CA) for 45 min. Cells were then washed and resuspended in 200 μL of PBS and then analyzed on a BD LSRII flow cytometer. All samples were analyzed in triplicate.

Endoscopic detection of adenomas in $Apc^{Pirc/+}$ rats:

Conscious six-month old female and male $Apc^{Pirc/+}$ rats (n=5) received intravenous injections of FSNs (30 fmol g^{-1}) via the tail vein using a tail-restrainer. The next day, the animals were anesthetized using inhalant isoflurane (Forane, Baxter, Deerfield, Il). The colons of the anesthetized animals were lavaged with phosphate-buffered saline (PBS). Endoscopy was performed with our custom-built combined NIRF/white-light (WL)/ imaging endoscopy system equipped with Spyglass fiberscope (Boston Scientific, Marlborough, MA), a 660-nm excitation laser operating at 10 mW (IBeamSmart, PT 70–75mW, Toptica Photonics AG, Gräfelfing, Germany), 664-nm long-pass filter (RazorEdge, LP02–664RU-25, Semrock, Rochester, NY), and an electron multiplying charge-coupled device (EMCCD) camera (Luca R, Andor Technology, Belfast, UK). For a detailed description of the combined NIRF/WL endoscopy systems, please see Figure S9. The colons

of the animals were surveilled and WL and NIRF imaging were concomitantly recorded using Captivate screen-capturing software (Adobe Inc, San Jose, CA). No video post-processing was performed with the exception of occasional adjustment of contrast- and brightness levels (applied to the full image). Following endoscopy, the animals were deeply anesthetized using inhalant isoflurane (Forane, Baxter, Deerfield, Il) and then euthanized via cervical dislocation. The intestinal tissues of the animals were immediately collected, rinsed with PBS and immediately imaged on a Pearl Trilogy NIRF imaging system. Upon completion of imaging (less then 10 minutes), the colonic tissues were immersion-fixed in neutral-buffered formalin (10% v/v) for 24 hours and processed for paraffin-embedding and H&E staining. H&E stained tissue sections (5-μm thickness) were imaged using a custom set-up inverted digital fluorescence microscope (DM6B Leica Biosystems, Buffalo Grove, Il) equipped with a highly sensitive Leica DFC9000GTIs camera (4.2M Pixel sCMOS camera), a Cy5.5 filter cube (49022-ET-Cy5.5; Chroma Technology Corp., Bellows Falls, VT), and a xenon arc lamp LB-LS/30 (Sutter Instrument) for NIRF imaging of FSNs. Image acquisition and processing were performed using LAS X software (Leica Biosystems)

Endoscopic detection of adenomas in $APC^{1311/+}$ pigs:

All experiments involving the $APC^{1311/+}$ pigs were performed in Germany. Sedated male $APC^{1311/+}$ pigs (18–21 months old; f=2) were injected intravenously with the FSNs (~4.5 pmol kg^{-1}) via a preplaced catheter into ear vein. The next day, the pigs were anesthetized by intramuscular (i.m.). injection of ketamine (20 mg kg^{-1} body weight) and azaperone (2 mg kg^{-1} body weight) and fluorescence-guided endoscopy was performed using a custom-built combined NIRF/WL endoscopy system equipped with a 670-nm laser and a ViZaar fiberscope (A250L2000; For detailed information see Figure S9c).[33] The animals that were euthanized were first sedated by i.m. administration of ketamine (20 mg kg^{-1} body weight) and azaperone (2 mg kg^{-1} body weight), rendered unconscious by a nonpenetrating captive bolt gun applied to the forehead and then immediately exsanguinated. Liver, spleen, kidney, colorectal tissues and muscle were harvested. The freshly resected colorectal tissues were randomly cut in sections of approximately 15 cm in length. All tissues were fixed in neutral-buffered formalin (10% v/v). The fixed tissue sections were imaged on a Pearl Trilogy NIRF imaging system and processed for paraffin-embedding and H&E staining.

Statistical analysis:

To calculate the tumor to background ratio (TBR), regions of interest (ROI) were drawn tightly around the tumor and on the tissue background. $TBR = ROI_{tumor} / ROI_{tissue\ background}$. Statistical analysis was performed in Excel (Microsoft). Detailed information on the sample size is described in the figure legends. All values in figures are presented as means ± SD unless otherwise noted in the text and figure legends. Statistical significance was calculated on the basis of the Student's t-test (two-tailed, unpaired), and the level of significance was set at least P values < 0.05.

Supplementary Material

Refer to Web version on PubMed Central for supplementary material.

Acknowledgements

Dr. S. Rogalla and Dr. K. Flisikowski contributed equally. This work was supported in part by the following grants: 1R01 CA182043-01A1 (S.S.G., C.H.C.), Will-Foundation Berlin (C.H.C., S.R., S.S.G.), Canary Center for Early Detection Seed Grant (S.R.), NCI CCNE U54 CA199075 (S.S.G.), Canary Foundation (S.S.G.), Deutsche Krebshilfe-Grant No. 111902 (A.S., K.F.), Deutsche Forschungsgemeinschaft SFB824 subprojects B5 and Z3 (D.G., V.N.). Part of this work was performed at the Stanford Nano Shared Facilities (SNSF), supported by the National Science Foundation under award ECCS-1542152. The authors thank the Comparative Medicine Animal Histology Service Center at Stanford University for providing histology services. We would like to thank Travis Shaffer for assisting in nanoparticle characterization. We also would like to thank Prof. Dr. Eben Rosenthal for generously allowing us to use his small-animal near-infrared fluorescence imaging systems and we would like to thank Carmel T. Chan for critically reviewing our manuscript.

References

[1]. Toll AD, Fabius D, Hyslop T, Pequignot E, DiMarino AJ, Infantolino A, Palazzo JP, Colorectal Dis 2011, 13, 370. [PubMed: 20718835]

[2]. (a)Zauber AG, Winawer SJ, O'Brien MJ, Lansdorp-Vogelaar I, van Ballegooijen M, Hankey BF, Shi W, Bond JH, Schapiro M, Panish JF, Stewart ET, Waye JD, N Engl J Med 2012, 366, 687; [PubMed: 22356322] (b)Tsai MH, Xirasagar S, Li YJ, de Groen PC, Prev Chronic Dis 2015, 12.

[3]. (a)Ahn SB, Han DS, Bae JH, Byun TJ, Kim JP, Eun CS, Gut Liver 2012, 6, 64; [PubMed: 22375173] (b)Leufkens AM, van Oijen MG, Vleggaar FP, Siersema PD, Endoscopy 2012, 44, 470; [PubMed: 22441756] (c)van Rijn JC, Reitsma JB, Stoker J, Bossuyt PM, van Deventer SJ, Dekker E, Am J Gastroenterol 2006, 101, 343. [PubMed: 16454841]

[4]. Corley DA, Jensen CD, Marks AR, Zhao WK, Lee JK, Doubeni CA, Zauber AG, de Boer J, Fireman BH, Schottinger JE, Quinn VP, Ghai NR, Levin TR, Quesenberry CP, N Engl J Med 2014, 370, 1298. [PubMed: 24693890]

[5]. (a)Zhan T, Hielscher T, Hahn F, Hauf C, Betge J, Ebert MP, Belle S, Digestion 2016, 93, 311; [PubMed: 27271329] (b)Friedland S, Shelton A, Kothari S, Kochar R, Chen A, Banerjee S, Diagn Ther Endosc 2013, 2013, 412936. [PubMed: 23761952]

[6]. (a)Marion JF, Waye JD, Israel Y, Present DH, Suprun M, Bodian C, Harpaz N, Chapman M, Itzkowitz S, Abreu MT, Ullman TA, McBride RB, Aisenberg J, Mayer L, Med MSS, Clin Gastroenterol H 2016, 14, 713;(b)Brown SR, Baraza W, Din S, Riley S, Cochrane Database Syst Rev 2016, 4, CD006439. [PubMed: 27056645]

[7]. Rastogi A, ASGE Leading Edge 2015, 5, 1.

[8]. Kuiper T, van den Broek FJ, Naber AH, van Soest EJ, Scholten P, Mallant-Hent R, van den Brande J, Jansen JM, van Oijen AH, Marsman WA, Bergman JJ, Fockens P, Dekker E, Gastroenterology 2011, 140, 1887. [PubMed: 21419769]

[9]. Harmsen S, Huang R, Wall MA, Karabeber H, Samii JM, Spaliviero M, White JR, Monette S, O'Connor R, Pitter KL, Sastra SA, Saborowski M, Holland EC, Singer S, Olive KP, Lowe SW, Blasberg RG, Kircher MF, Sci Transl Med 2015, 7, 271ra7.

[10]. Harmsen S, Rogalla S, Huang R, Spaliviero M, Neuschmelting V, Hayakawa Y, Lee Y, Tailor Y, Toledo-Crow R, Kang JW, Samii JM, Karabeber H, Davis RM, White JR, van de Rijn M, Gambhir SS, Contag CH, Wang T, Kircher MF, ACS Nano 2019, DOI: 10.1021/acsnano.8b06808.

[11]. Perry JL, Reuter KG, Kai MP, Herlihy KP, Jones SW, Luft JC, Napier M, Bear JE, DeSimone JM, Nano Lett 2012, 12, 5304. [PubMed: 22920324]

[12]. Meng F, Engbers GH, Feijen J, J Biomed Mater Res A 2004, 70, 49. [PubMed: 15174108]

[13]. (a)Moser AR, Mattes EM, Dove WF, Lindstrom MJ, Haag JD, Gould MN, P Natl Acad Sci USA 1993, 90, 8977;(b)Moser AR, Pitot HC, Dove WF, Science 1990, 247, 322. [PubMed: 2296722]

[14]. (a)Amos-Landgraf JM, Kwong LN, Kendziorski CM, Reichelderfer M, Torrealba J, Weichert J, Haag JD, Chen KS, Waller JL, Gould MN, Dove WF, P Natl Acad Sci USA 2007, 104, 4036; (b)Washington MK, Powell AE, Sullivan R, Sundberg JP, Wright N, Coffey RJ, Dove WF, Gastroenterology 2013, 144, 705. [PubMed: 23415801]

[15]. Flisikowska T, Merkl C, Landmann M, Eser S, Rezaei N, Cui X, Kurome M, Zakhartchenko V, Kessler B, Wieland H, Rottmann O, Schmid RM, Schneider G, Kind A, Wolf E, Saur D, Schnieke A, Gastroenterology 2012, 143, 1173. [PubMed: 22864254]

[16]. Flisikowska T, Stachowiak M, Xu H, Wagner A, Hernandez-Caceres A, Wurmser C, Perleberg C, Pausch H, Perkowska A, Fischer K, Frishman D, Fries R, Switonski M, Kind A, Saur D, Schnieke A, Flisikowski K, Sci Rep 2017, 7, 6613. [PubMed: 28747659]

[17]. Nair AB, Jacob S, J Basic Clin Pharm 2016, 7, 27. [PubMed: 27057123]

[18]. Nguyen QT, Tsien RY, Nat Rev Cancer 2013, 13, 653. [PubMed: 23924645]

[19]. Imaizumi K, Harada Y, Wakabayashi N, Yamaoka Y, Konishi H, Dai P, Tanaka H, Takamatsu T, Gastrointest Endosc 2012, 75, 110. [PubMed: 22032849]

[20]. (a)Hartmans E, Tjalma JJJ, Linssen MD, Allende PBG, Koller M, Jorritsma-Smit A, Nery M, Elias SG, Karrenbeld A, de Vries EGE, Kleibeuker JH, van Dam GM, Robinson DJ, Ntziachristos V, Nagengast WB, Theranostics 2018, 8, 1458; [PubMed: 29556334] (b)Burggraaf J, Kamerling IM, Gordon PB, Schrier L, de Kam ML, Kales AJ, Bendiksen R, Indrevoll B, Bjerke RM, Moestue SA, Yazdanfar S, Langers AM, Swaerd-Nordmo M, Torheim G, Warren MV, Morreau H, Voorneveld PW, Buckle T, van Leeuwen FW, Odegardstuen LI, Dalsgaard GT, Healey A, Hardwick JC, Nat Med 2015, 21, 955. [PubMed: 26168295]

[21]. (a)Hsiung PL, Hardy J, Friedland S, Soetikno R, Du CB, Wu AP, Sahbaie P, Crawford JM, Lowe AW, Contag CH, Wang TD, Nat Med 2008, 14, 454; [PubMed: 18345013] (b)Sensarn S, Zavaleta CL, Segal E, Rogalla S, Lee W, Gambhir SS, Bogyo M, Contag CH, Mol Imaging Biol 2016, 18, 820. [PubMed: 27154508]

[22]. (a)Bansal A, Liu X, McGregor DH, Singh V, Hall S, Am J Med Sci 2010, 340, 296; [PubMed: 20622650] (b)Tjalma JJ, Garcia-Allende PB, Hartmans E, van Scheltinga AGT, Boersma-van Ek W, Glatz J, Koch M, van Herwaarden YJ, Bisseling TM, Nagtegaal ID, Timmer-Bosscha H, Koornstra JJ, Karrenbeld A, Kleibeuker JH, van Dam GM, Ntziachristos V, Nagengast WB, J Nucl Med 2016, 57, 480. [PubMed: 26678613]

[23]. Rex DK, Kahi C, O'Brien M, Levin TR, Pohl H, Rastogi A, Burgart L, Imperiale T, Ladabaum U, Cohen J, Lieberman DA, Gastrointest Endosc 2011, 73, 419. [PubMed: 21353837]

[24]. Duncan R, Nat Rev Drug Discov 2003, 2, 347. [PubMed: 12750738]

[25]. Matsumura Y, Maeda H, Cancer Res 1986, 46, 6387. [PubMed: 2946403]

[26]. Theek B, Gremse F, Kunjachan S, Fokong S, Pola R, Pechar M, Deckers R, Storm G, Ehling J, Kiessling F, Lammers T, J Control Release 2014, 182, 83. [PubMed: 24631862]

[27]. (a)Bossi P, Viale G, Lee AK, Alfano R, Coggi G, Bosari S, Cancer Res 1995, 55, 5049; [PubMed: 7585550] (b)Takeda K, Kudo SE, Mori Y, Misawa M, Kudo T, Wakamura K, Hayashi T, Miyachi H, Ishida F, Inoue H, Oncol Lett 2016, 11, 237. [PubMed: 26870195]

[28]. Phillips E, Penate-Medina O, Zanzonico PB, Carvajal RD, Mohan P, Ye Y, Humm J, Gonen M, Kalaigian H, Schoder H, Strauss HW, Larson SM, Wiesner U, Bradbury MS, Sci Transl Med 2014, 6, 260ra149.

[29]. Harmsen S, Bedics MA, Wall MA, Huang R, Detty MR, Kircher MF, Nat Commun 2015, 6, 6570. [PubMed: 25800697]

[30]. Ow H, Larson DR, Srivastava M, Baird BA, Webb WW, Wiesner U, Nano Lett 2005, 5, 113. [PubMed: 15792423]

[31]. Young M, Ordonez L, Clarke AR, Mol Oncol 2013, 7, 178. [PubMed: 23465602]

[32]. Cho KR, Vogelstein B, Cancer 1992, 70, 1727. [PubMed: 1516027]

[33]. Glatz J, Varga J, Garcia-Allende PB, Koch M, Greten FR, Ntziachristos V, J Biomed Opt 2013, 18, 101302. [PubMed: 23797876]

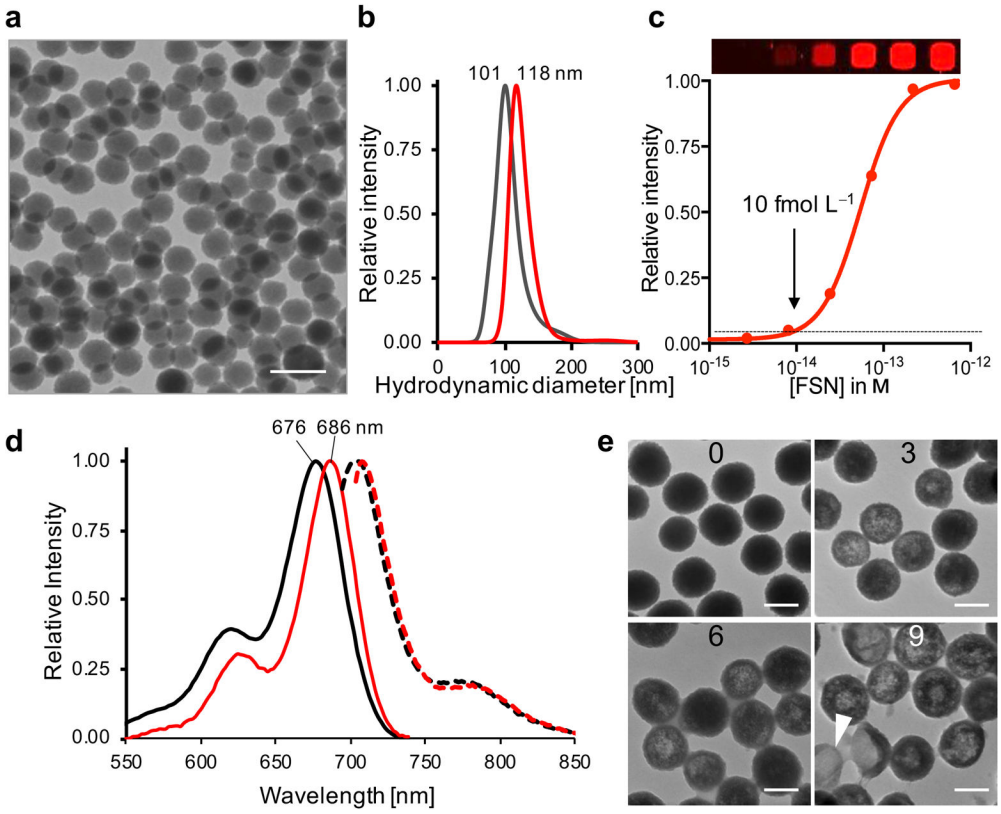

Figure 1. FSN characterization.

a) Transmission electron microscopy (TEM) images of FSNs. Scale bar, 200 nm. b) Nanoparticle tracking analysis (NTA) of 1.0 pM bare FSN cores and PEGylated FSNs (FSN-PEG-OH) in water. c) Limit of detection (LOD) of FSNs is 10 fM (10×10^{-15} M; threshold was arbitrarily set at 0.05 relative intensity (---)). d) Excitation and emission (λ_{ex} 680 nm; (---)) curves of CF680R-MPTMS (black) and FSNs (red) in ethanol. e) TEM images of 1 nM FSNs incubated in 50% (w/v) human serum at 37 °C for 0, 3, 6, or 9 d. The FSNs start to etch from the inside and then collapse (arrow head; day 9). Scale bar, 100 nm.

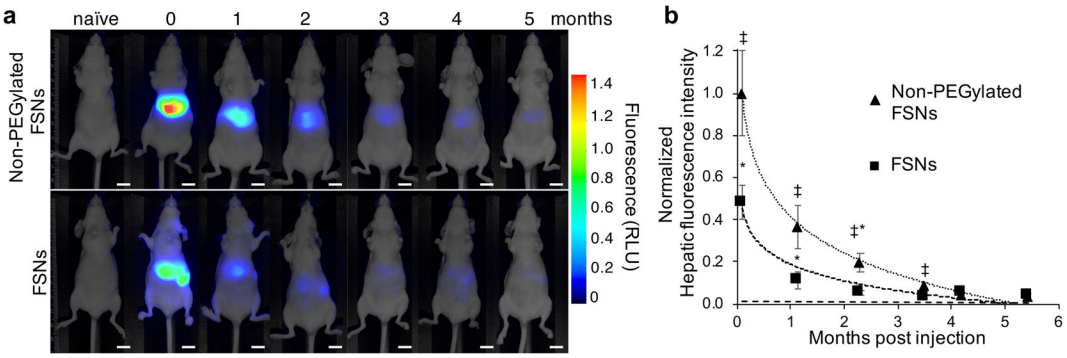

Figure 2. Biodegradability of non-PEGylated FSNs and FSNs *in vivo*.

a) Whole-body fluorescence imaging of naïve nude mice (n=5) and 1 d (0 months) and consequent months post intravenous injection of non-PEGylated FSNs (30 fmol g^{-1}; n=5) or FSNs (30 fmol g^{-1}; n=5). Fluorescence intensity is expressed in arbitrary units. Scale bar, 1 cm. b) Plot of the normalized hepatic fluorescence signal post injection of non-PEGylated FSN (R^2 = 0.9962; $t_{1/2}$ 3.0 weeks) or FSNs (R^2 = 0.9374; $t_{1/2}$ 2.7 weeks) versus the average fluorescence background intensity of the liver in naïve nude mice (---). Data represents mean ±SD. $^{‡}P$<0.001, non-PEGylated FSN versus naïve; *P<0.001, FSN versus naïve.

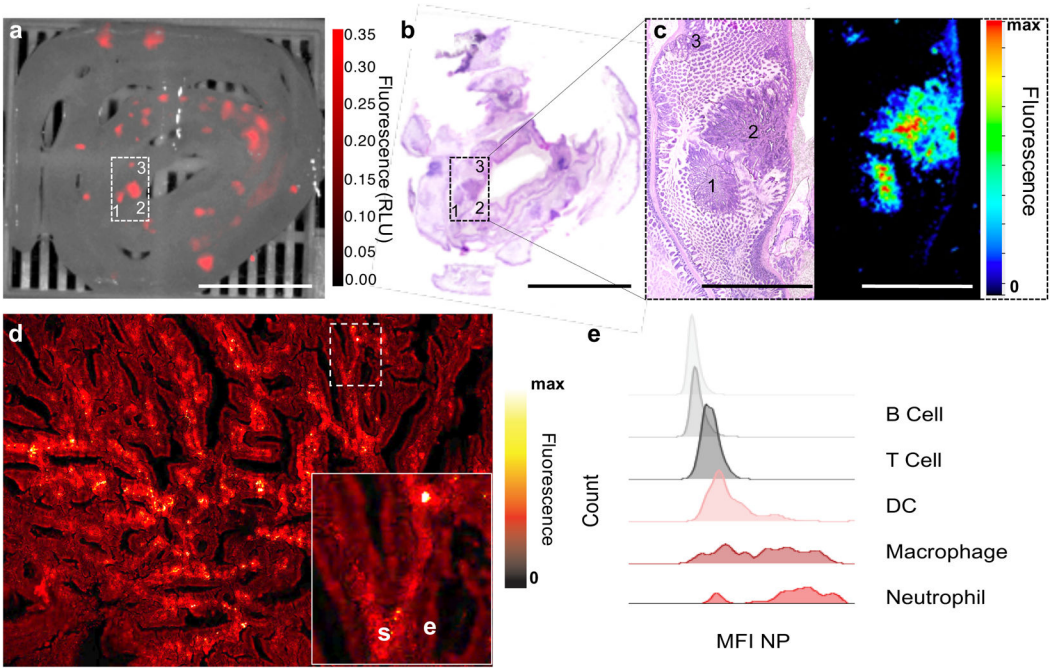

Figure 3. Gastrointestinal tumor accumulation of FSNs in *Apc*$^{Min/+}$ mice.

a) Near-infrared (NIR) fluorescence imaging (λ_{ex} 680 nm; λ_{em} >700 nm) was performed on freshly resected ileal tissues of *Apc*$^{Min/+}$ mice that had received FSNs (i.v. 30 fmol g^{-1}; n=5). Tumor-to-background ratios (TBR) were 4.0, 3.6, 3.0 for polyps 1–3, respectively. Fluorescence intensity is displayed in arbitrary units. Scale bar, 10 mm. b) H&E stained tissue section (15-μm). Scale bar, 10 mm. c) 4× magnification and NIR fluorescence imaging of the selected area (panel (a) and (b)) showing that the fluorescence signal of the FSNs aligns well with polyps 1–3. Scale bar, 2.5 mm. d) 20× magnification NIRF microscopy imaging (λ_{ex} 680 nm; λ_{em} >700 nm) of the polyp in panel (c) demonstrates the fluorescent nanoparticles mainly localized to the tumor stroma ('s') and not to epithelial cells ('e'). Inset is a 4× higher magnification of the indicated area. e) Fluorescence-activated cell sorting (FACS) analysis of the polyps of *Apc*$^{Min/+}$ mice (n=2) showed that the mean fluorescence intensity (MFI) of the FSNs was mainly associated with macrophages and neutrophils. See also Figure S8.

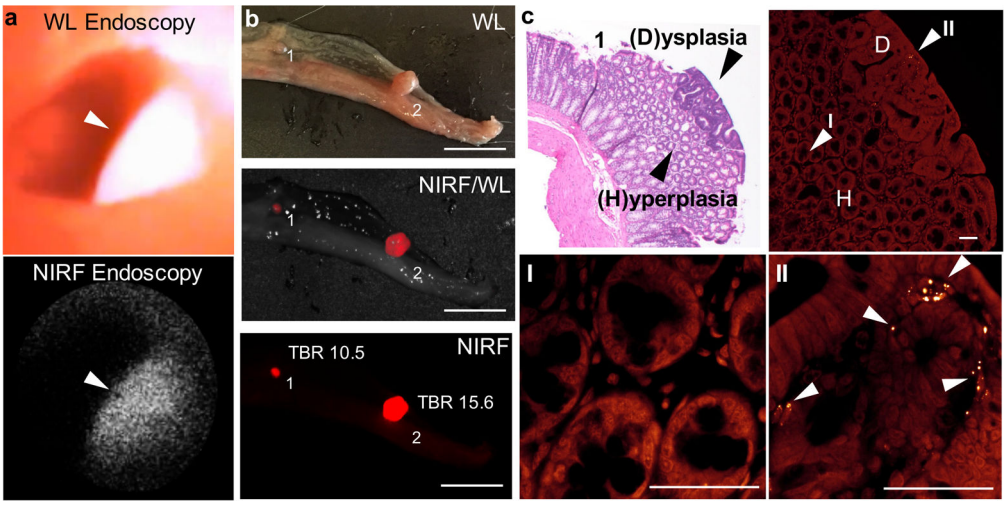

Figure 4. FSN-augmented combined NIRF/WL endoscopy in *Apc*$^{Pirc/+}$ rats.

a) A protruding adenoma was visualized with high sensitivity using NIRF endoscopy (λ_{ex} 660 nm; λ_{em} >664 nm). b) *Ex vivo* wide-field NIRF imaging (λ_{ex} 680 nm; λ_{em} >700 nm) of a freshly resected open colon from an *Apc*$^{Pirc/+}$ rat (n=5) that had received i.v. injection of FSNs (30 fmol g^{-1}) corroborated the presence of adenomas of mixed morphology and re-emphasized the high sensitivity (TBR>10) of FSN-augmented NIRF (endoscopic) imaging. Scale bars, 10 mm. c) H&E (top left panel) and confocal NIRF microscopy (top right panel) of adenoma 1 (panel (b)) demonstrated that the granular NIRF signal of the FSNs (II; white arrow heads) co-localizes with the basophilic tumor area on the H&E stained 5-μm thick tissue section (dysplastic tissue ('D'); II) and is not associated with normal or hyperplastic tissue ('H'; I). Scale bars, 50 μm. See also Figure S10 and Movie S1.

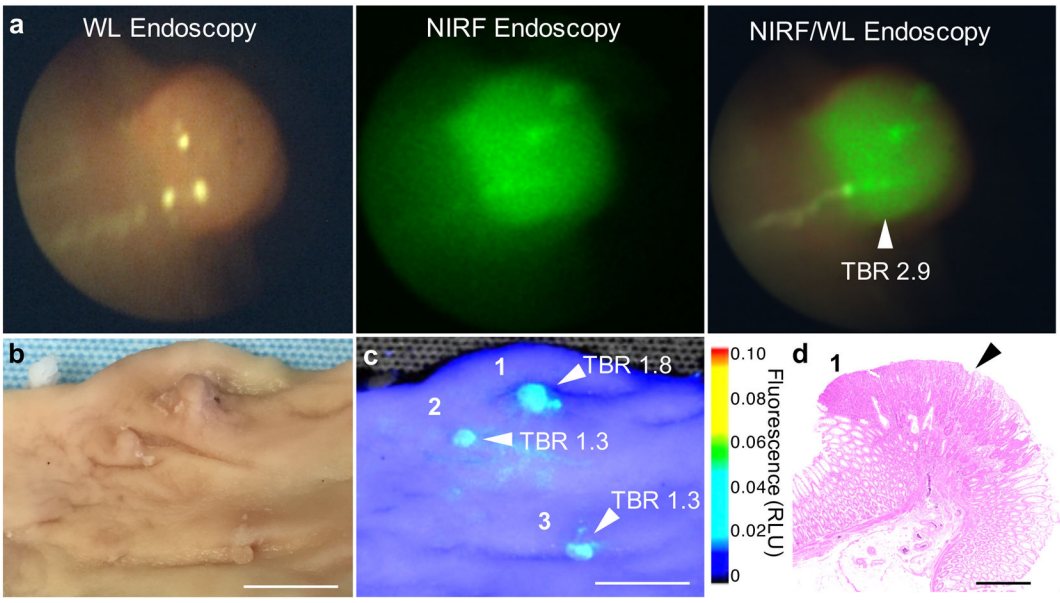

Figure 5. FSN-augmented combined NIRF/WL endoscopy in *APC*$^{1311/+}$ pigs.

a) White-light (left panel), NIRF (middle panel), and combined NIRF/WL (right panel) endoscopic images of a colorectal polyp in *APC*$^{1311/+}$ pigs (n=2) 18 h after intravenous administration of FSNs (4.7 pmol kg^{-1}). b) White-light, and c) wide-field NIRF imaging (λ_{ex} 680 nm; λ_{em} >700 nm) of a randomly resected colorectal tissue section from the scoped *APC*$^{1311/+}$ pig. Fluorescence intensity is expressed as arbitrary units. Scale bar, 10 mm. d) Representative H&E stained section of a NIRF-positive lesions corroborated the presence of adenomatous polyps (black arrowhead). Scale bar, 1 mm. See also Movie S2.